Supplementary Information to "High-resolution and Wide-frequency-range Magnetic Spectroscopy with Solid-state Spin Ensembles"

Zechuan Yin,[1,2,*] Justin J. Welter,[1,2] Connor A. Hart,[1,2] Paul V. Petruzzi,[3] and Ronald L. Walsworth[1,2,4,†]

[1] *Department of Electrical and Computer Engineering, University of Maryland, College Park, Maryland 20742, USA*
[2] *Quantum Technology Center, University of Maryland, College Park, Maryland 20742, USA*
[3] *Laboratory for Physical Sciences, 8050 Greenmead Dr, College Park, Maryland 20740, USA*
[4] *Department of Physics, University of Maryland, College Park, Maryland 20742, USA*

Contents

I. Experimental Details 1

II. Rotating Frame Hamiltonian Approximation in the Floquet Picture 2

III. Fourier Analysis of QFM-CASR Signal 4

IV. AC Bias Field Calibration, Target Signal Sensitivity Measurement, and Bias Field Polarization 5

V. Effective Signal Validation with Rabi and DEER-Rabi 7

VI. Phase Measurements of Arbitrary Frequency Signals 10

VII. Comparison of NV-Diamond AC Sensing Techniques 10

VIII. Demonstration of Sub-Hz QFM-CASR Spectral Resolution 12

IX. Demonstration of QFM-CASR at 2.5 MHz AC Bias Field Detuning 12

X. QFM-CASR Performance Limitations, Trade-Offs, and Optimization 13

XI. Assessment of QFM-CASR Applied to Tesla-Scale NMR of Micron-Scale Samples 14

References 15

Supplementary Note I: Experimental Details

The $2 \times 2 \times 0.5\,\mathrm{mm}^3$ high-purity diamond substrate used in this work was produced by Element Six Ltd (E6) and features an $1.7\,\mu$m-thick NV layer, created by growing a ^{15}N-enriched CVD layer of NV centers ([N] = 17 ppm, $> 99.99\%$ ^{12}C) with post-growth treatment via electron irradiation and annealing increasing the NV concentration to 2.7 ppm. Sides of the diamond are polished to allow for efficient total internal reflection (TIR) coupling of 532 nm light, generated by a diode-pumped solid-state laser (Lighthouse Photonics, Sprout-H). The laser beam is focused through an acousto-optic modulator (AOM) (Gooch & Housego, Model 3250-220) with a $f = 500$ mm spherical convex lens, where the first-order diffracted beam is shaped by an $f = 130$ mm cylindrical convex lens and a $f = 100$ mm spherical convex lens to produce an elliptical beam profile focused onto one of the aforementioned polished side surfaces of the diamond sample. We estimate approximately 2.5W of laser power is incident to the diamond to illuminate a $\sim 400 \times 600\,\mu$m area of the NV layer. Optical pulses are controlled by gating the AOM's input RF power with a switch (Mini-Circuits, ZASWA-2-50DR+) that is controlled by transistor-transistor logic (TTL) pulses from the marker channel of an arbitrary waveform generator (AWG, Zurich Instruments, SHFSG). The resulting NV spin-state-dependent photoluminesence (PL), see Fig. S1(a), is collected by a $20\times/0.75$ NA Nikon objective, where

* zcyin@umd.edu
† walsworth@umd.edu

it is separated from the illuminating laser light by a 647 nm long-pass filter (Semrock), clipped by an iris so as to collect only the PL from NV centers in a primarily homogeneous laser-illumination region given by an approximately $\sim 20\,\mu$m diameter area on the diamond, and focused onto a photodiode (Thorlabs, PDA36A2). The photodiode's output voltage is then acquired using a DAQ system (National Instruments, NI USB6259).

All microwave (MW) and radio frequency (RF) signals and pulses, including those used for driving NV electronic spins (e.g., with XY8-k sequences), application of target RF signal and AC bias fields, and introduction of test signals, are generated by a four-channel AWG (Zurich Instruments, SHFSG). The signal and bias channels are merged using a combiner (Mini-Circuits ZFRSC-42-S+) before being fed into a single amplifier selected for frequency range: Mini-circuits LZY-22+ (0.1 MHz to 200 MHz, ZHL-50W-52-S+ (50 MHz to 500 MHz), and ZHL-15W-422-S+ (600 MHz to 4.2 GHz)). The NV drive uses a separate designated amplifier (Mini-Circuits ZHL-16W-43-S+).

The NV drive MW signal is delivered by a small-loop antenna ("MW loop") fabricated as a 300 nm-thick, 800 μm inner diameter gold Ω-pattern onto a SiC wafer. The diamond is glued onto the SiC wafer for mechanical stability. The target RF and AC bias signals are applied by a custom-made coaxial shorted loop antenna ("RF coil") with a diameter of approximately 1 mm. A static bias magnetic field of approximately 21.7 mT at the NV layer is generated by four pairs of temperature-compensated, permanent samarium cobalt ring magnets, with the field aligned along one of the four NV ensemble axes.

Supplementary Note II: Rotating Frame Hamiltonian Approximation in the Floquet Picture

Following the analysis of the quantum frequency mixing (QFM) effect introduced in [1], we model the NV electronic spin ground state as a two-level Hamiltonian H_0 simplified to include only one resonant transition from $m_s = 0$ to $m_s = +1$ or $m_s = -1$ with transition frequency ω_0:

$$H_0 = \frac{\omega_0}{2}\sigma_z. \tag{S1}$$

The interaction Hamiltonian representing the effect of both an AC bias field and target RF signal field, denoted H_b and H_s respectively, is given by:

$$H_{int} = H_b + H_s. \tag{S2}$$

We consider the case where both the AC bias field and signal field are far detuned from the NV spin transition ω_0 and linearly polarized transverse to the NV $\hat{z}$ axis, e.g., linearly polarized in $\hat{x}$, so that the relevant bias and signal Hamiltonians are given by:

$$H_{b,s} = \Omega_{b,s}\cos\left(\omega_{b,s} + \phi_{b,s}\right)\sigma_x, \tag{S3}$$

where $\Omega_{b,s}$ and $\omega_{b,s}$ are the amplitude and frequency of the bias or signal fields, respectively. The total Hamiltonian of the system in the laboratory frame is:

$$H = \frac{\omega_0}{2}\sigma_z + \Omega_s\cos\left(\omega_s + \phi_s\right)\sigma_x + \Omega_b\cos\left(\omega_b + \phi_b\right)\sigma_x. \tag{S4}$$

We then transform into a rotating frame described by the frequency ω_0 with the unitary $U = e^{-i(\omega_0 t/2)\sigma_z}$, such that the Hamiltonian in the rotating frame is given by:

$$\tilde{H} = U^\dagger H U + i\frac{\partial U^\dagger}{\partial t}U. \tag{S5}$$

See Fig. S1(b). Since $U^\dagger H_0 U + i(\partial U^\dagger/\partial t)U = 0$, $\tilde{H} = U^\dagger H_{int} U$. Applying the rotating frame transformation to the AC bias field and signal field Hamiltonians, we obtain:

$$\tilde{H}_{b,s} = U^\dagger H_{b,s} U = \frac{\Omega_{b,s}}{2}(e^{i(\omega_{b,s}t+\phi_{b,s})} + e^{-i(\omega_{b,s}t+\phi_{b,s})})(e^{i\omega_0 t}\sigma_+ + e^{-i\omega_0 t}\sigma_-). \tag{S6}$$

The total system Hamiltonian in the rotating frame, $\tilde{H} = \tilde{H}_b + \tilde{H}_s$, is then given by:

$$\begin{aligned}
\tilde{H} = &\frac{\Omega_b}{2}\left(\cos\left([\omega_b - \omega_0]t + \phi_b\right)\sigma_x + \sin\left([\omega_b - \omega_0]t + \phi_b\right)\sigma_y\right) \\
&+ \frac{\Omega_b}{2}\left(\cos\left([\omega_b + \omega_0]t + \phi_b\right)\sigma_x - \sin\left([\omega_b + \omega_0]t + \phi_b\right)\sigma_y\right) \\
&+ \frac{\Omega_s}{2}\left(\cos\left([\omega_s - \omega_0]t + \phi_s\right)\sigma_x + \sin\left([\omega_s - \omega_0]t + \phi_s\right)\sigma_y\right) \\
&+ \frac{\Omega_s}{2}\left(\cos\left([\omega_s + \omega_0]t + \phi_s\right)\sigma_x - \sin\left([\omega_s + \omega_0]t + \phi_s\right)\sigma_y\right).
\end{aligned} \tag{S7}$$

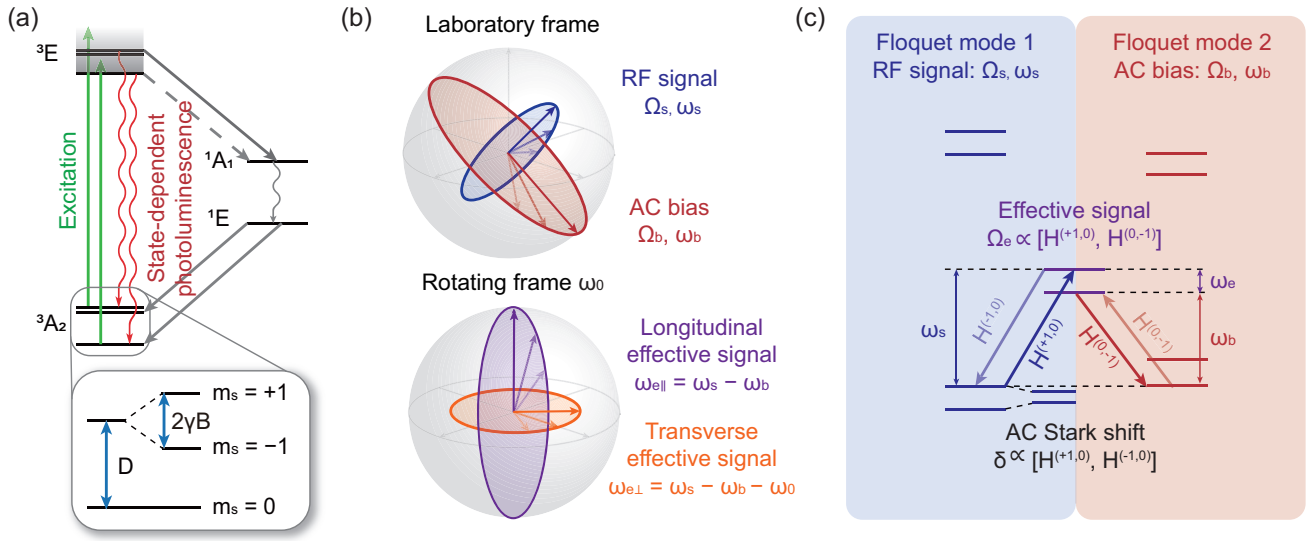


FIG. S1. (a) Detailed NV$^-$ energy-level diagram. The negatively charged NV center in diamond exhibits an electronic spin triplet ground state and excited state. A non-radiative decay channel via an inter-system crossing (ISC) results in spin-state-dependent photoluminescence (PL) and preferential occupation of the $m_s = |0\rangle$ ground state in the presence of green light illumination. (b) Bloch sphere visualization of the AC bias, target RF signal, and effective signal fields in both the laboratory and rotating frames, illustrating the general case. In the present work, the XY8 sequence is primarily sensitive to the longitudinal effective signal; and the RF signal and AC bias fields are linearly polarized and generated by the same coil, and hence are colinear in the laboratory frame. Thus, we consider only the x-component of the RF signal and AC bias fields, which contribute to the longitudinal effective signal, to simplify the Hamiltonian model. (c) Simplified schematic of quantum frequency mixer (QFM) dynamics, including the effective signal amplitude Ω_e and AC Stark shift δ mediated by virtual Floquet modes.

This Hamiltonian describes a four-mode Floquet problem, with frequency modes $(\omega_b - \omega_0)$, $(\omega_b + \omega_0)$, $(\omega_s - \omega_0)$, $(\omega_s + \omega_0)$. To simplify the analysis for the regime relevant to our experiment, we first consider the two-mode Floquet problem; see Fig. S1(c). For a time-dependent Hamiltonian $H(t)$ with two uncoupled frequency modes ω_1 and ω_2 of evolution amplitudes Ω_1 and Ω_2, the Fourier expansion is given by:

$$H(t) = \sum_{n=-\infty}^{\infty} \sum_{k=-\infty}^{\infty} H^{(n,k)} e^{in\omega_1 t} e^{ik\omega_2 t}. \tag{S8}$$

We can write $H(t)$ as a Floquet Hamiltonian H_F in the Floquet space, using the ladder operators $F_{n,k}^{\omega_{1,2}}$ and the number operator F_z:

$$H_F = \sum_{n=-\infty}^{\infty} \sum_{k=-\infty}^{\infty} \left(H^{(n,k)} \otimes F_n^{\omega_1} \otimes F_k^{\omega_2} + \omega_1 I \otimes F_z^{\omega_1} \otimes I + \omega_2 I \otimes I \otimes F_z^{\omega_2} \right). \tag{S9}$$

We then approximately diagonalize H_F by transforming with unitary $U = e^S$ for Hermitian operator S, and apply the Baker–Campbell–Hausdorff (BCH) expansion for the infinitesimal case:

$$\tilde{H}_F = e^S H_F e^{-S} = H_F + [S, H_F] + \frac{1}{2}[S, [S, H_F]] + ... \tag{S10}$$

With an appropriate choice of S, the off-diagonal terms can be made to cancel to first order; and the second order term can be simplified so that transformation back to the Hilbert space yields the second order term [1]:

$$H_2^{(m,h)} = -\frac{1}{2} \sum_{n,k} \frac{[H^{(m-n,h-k)}, H^{(n,k)}]}{n\omega_1 + k\omega_2}. \tag{S11}$$

As the fast-oscillating terms quickly average to zero, we consider only the cases where the integer pairs (m, h) satisfy $m\omega_1 + h\omega_2 \ll \omega_3$, for $\omega_3 \in \{n\omega_1 + k\omega_2 \,|\, n, k \in \mathbb{Z},\ n\omega_1 + k\omega_2 \neq 0,\ H^{(n,k)} \neq 0\}$. When the amplitudes $\Omega_1, \Omega_2 \ll \omega_1, \omega_2$,

the system dynamics are then well approximated by a single effective Hamiltonian given by:

$$H(t) = \frac{1}{2}\left(\frac{1}{\omega_1} - \frac{1}{\omega_2}\right)[H_1, H_2]e^{i(\omega_1+\omega_2)t}. \tag{S12}$$

We now apply the above analysis to the four-mode Floquet problem assuming $\Omega_b, \Omega_s \ll \omega_b, \omega_s$ so that we can truncate at second order. The resulting Hamiltonian includes all possible sums and differences of the four frequency modes $(\omega_b - \omega_0)$, $(\omega_b + \omega_0)$, $(\omega_s - \omega_0)$, $(\omega_s + \omega_0)$. However, we also assume $|\omega_s - \omega_b| \ll (\omega_b + \omega_s), \omega_0$ and make the rotating wave approximation to neglect fast oscillating terms. Thus, only the $|\omega_s - \omega_b|$ and DC terms survive in the effective Hamiltonian:

$$\begin{aligned}\tilde{H}_e = -\left(\frac{\omega_0}{\omega_b^2 - \omega_0^2} + \frac{\omega_0}{\omega_s^2 - \omega_0^2}\right)\frac{\Omega_b\Omega_s}{2}\frac{e^{i[(\omega_s-\omega_b)t+(\phi_s-\phi_b)]} + e^{-i[(\omega_s-\omega_b)t+(\phi_s-\phi_b)]}}{2}\sigma_z \\ + \left(-\frac{\Omega_b^2\omega_0}{2(\omega_b^2 - \omega_0^2)} - \frac{\Omega_s^2\omega_0}{2(\omega_s^2 - \omega_0^2)}\right)\sigma_z.\end{aligned} \tag{S13}$$

We define the effective signal at frequency $\omega_e = \omega_s - \omega_b$, with phase $\phi_e = \phi_s - \phi_b$, effective amplitude Ω_e, and AC Stark shift δ:

$$\Omega_e = \frac{\Omega_b\Omega_s}{2}\left(\frac{\omega_0}{\omega_b^2 - \omega_0^2} + \frac{\omega_0}{\omega_s^2 - \omega_0^2}\right), \tag{S14}$$

$$\delta = \left(-\frac{\Omega_b^2\omega_0}{\omega_b^2 - \omega_0^2} - \frac{\Omega_s^2\omega_0}{\omega_s^2 - \omega_0^2}\right). \tag{S15}$$

The effective interaction Hamiltonian in the rotating frame is that of an applied longitudinal field with amplitude Ω_e at frequency ω_e:

$$\tilde{H}_e = \frac{\delta}{2}\sigma_z + \Omega_e \cos(\omega_e t + \phi_e)\sigma_z. \tag{S16}$$

We note the asymptotic behavior of Ω_e tends towards $\frac{\Omega_b\Omega_s}{\omega_0}$ in the low frequency limit for ω_s and ω_b and towards $\frac{\Omega_b\Omega_s\omega_0}{\omega_s^2}$ in the ultra-high frequency limit, assuming $\omega_b \approx \omega_s$.

We also note that driving an NV electronic spin transition with a strong field $\Omega_0 \cos(\omega_0 t)\sigma_x$, as part of a dynamical decoupling sensing protocol (XY8-6 in this work), induces a Bloch-Siegert shift of the effective signal frequency given by $\frac{\Omega_0}{8\omega_0}$ [1]. Since the NV resonance frequency ω_0 is typically on the order of GHz, while the microwave field amplitude Ω_0 is on the order of MHz, this static shift is much smaller than the CASR detection bandwidth employed in this work and hence has insignificant effect on calibration of the QFM-CASR protocol.

Supplementary Note III: Fourier Analysis of QFM-CASR Signal

In this work, we integrate the QFM effect with the coherently averaged synchronized readout (CASR) protocol [2] to sense the longitudinal effective signal described by Eq. (S16) above. A continuous envelope function describing the normalized time-domain QFM-CASR PL signal is given by [3]:

$$\begin{aligned}S(t, \Omega_e, \phi_e) =& \frac{1}{2}\{1 + \sin[\kappa\Omega_e \cos(\omega_e t + \phi_e)]\} \\ =& \frac{1}{2} + \frac{1}{2}\sum_{n=0}^{\infty}(-1)^n J_{2n+1}(\kappa\Omega_e)\cos[(2n+1)(\omega_e t + \phi_e)],\end{aligned} \tag{S17}$$

where $\kappa = 4\pi N/\omega_e$ is a constant, N is the number of π pulses in each dynamical decoupling sensing sequence (N = 48 for the XY8-6 sequence used in the present experiment), and $J_n(x)$ is the n-th order Bessel function. The QFM-CASR spectrum after an FFT of Eq. (S17) is given by:

$$\begin{aligned}S_{\mathrm{CASR}}(\omega, \Omega_e, \phi_e) =& \frac{\sqrt{2\pi}}{2}\{\delta(\omega) + \pi\sum_{n=0}^{\infty}(-1)^n J_{2n+1}(\kappa\Omega_e)[e^{-i\phi_e}\delta(\omega - (2n+1)\omega_e) + e^{i\phi_e}\delta(\omega + (2n+1)\omega_e)]\} \\ =& S_{\mathrm{DC}} + S_{\mathrm{Real}} + iS_{\mathrm{Imag}},\end{aligned} \tag{S18}$$

where $\delta(\omega)$ is the Dirac function in frequency space; and S_{DC}, S_{Real}, and S_{Imag} are the DC component, real part, and imaginary part of the Fourier spectrum. $S_{\mathrm{DC}} = \frac{\sqrt{2\pi}}{2}\delta(\omega)$; and the real and imaginary parts are given by:

$$\begin{aligned} S_{\mathrm{Real}}(\omega, \Omega_e, \phi_e) &= \sqrt{2\pi^3}\cos(\phi_e)\sum_{n=0}^{\infty}(-1)^n J_{2n+1}(\kappa\Omega_e)[\delta(\omega+(2n+1)\omega_e)+\delta(\omega-(2n+1)\omega_e)], \\ S_{\mathrm{Imag}}(\omega, \Omega_e, \phi_e) &= \sqrt{2\pi^3}\sin(\phi_e)\sum_{n=0}^{\infty}(-1)^n J_{2n+1}(\kappa\Omega_e)[\delta(\omega+(2n+1)\omega_e)-\delta(\omega-(2n+1)\omega_e)]. \end{aligned} \tag{S19}$$

In this experiment, we ensure $\Omega_e \ll \omega_e$, leading to $\kappa\Omega_e \ll 1$; hence we can ignore the contribution of higher order Bessel functions. Keeping the first order Bessel term and the positive part due to the symmetry of the Fourier spectrum, the real and imaginary parts can be simplified as:

$$\begin{aligned} S^{+}_{\mathrm{Real}}(\omega, \Omega_e, \phi_e) &= \sqrt{2\pi^3}\cos(\phi_e)J_1(\kappa\Omega_e)\delta(\omega-\omega_e), \\ S^{+}_{\mathrm{Imag}}(\omega, \Omega_e, \phi_e) &= -\sqrt{2\pi^3}\sin(\phi_e)J_1(\kappa\Omega_e)\delta(\omega-\omega_e). \end{aligned} \tag{S20}$$

In the experiment, the QFM-CASR PL signal is read out at discrete intervals $t = n \cdot t_{\mathrm{Seq}}$, where $n = 1, 2, 3...$ are integers, and t_{Seq} is the total sequence length for one CASR PL data acquisition (including signal and reference, each consists of NV initialization and readout, and one application of the XY8-6 protocol) . The CASR sampling rate $\omega_{\mathrm{SR}} = 2\pi/t_{\mathrm{Seq}}$. Based on Nyquist–Shannon sampling theorem, the bandwidth of the measured Fourier spectrum is $\omega_{\mathrm{SR}}/2$. The alias frequency of QFM-CASR measurements of the effective signal is $\omega_a = \mid \omega - m\omega_{\mathrm{SR}} \mid$, where m is the integer closest to $\omega_e/\omega_{\mathrm{SR}}$. Consequently, the measured real and imaginary components of the QFM-CASR spectrum are:

$$\begin{aligned} S^{+}_{\mathrm{Real,m}}(\omega, \Omega_e, \phi_e) &= \sqrt{2\pi^3}\cos(\phi_e)J_1(\kappa\Omega_e)\delta(\omega-\omega_a), \\ S^{+}_{\mathrm{Imag,m}}(\omega, \Omega_e, \phi_e) &= -\sqrt{2\pi^3}\sin(\phi_e)J_1(\kappa\Omega_e)\delta(\omega-\omega_a). \end{aligned} \tag{S21}$$

The QFM-CASR spectrum amplitude of the effective signal is thus given by:

$$S_{\mathrm{CASR}} = S^{+}_{\mathrm{Amp,m}}(\omega, \Omega_e) = \sqrt{2\pi^3}J_1(\kappa\Omega_e)\delta(\omega-\omega_a). \tag{S22}$$

As noted above for this experiment, $\kappa\Omega_e \ll 1$, such that the first-order Bessel function can be approximated as linear, and thus $S_{\mathrm{CASR}} \propto \Omega_e$. To determine the effective signal phase ϕ_e, we can calculate the ratio of the measured components given in equation (S21) as:

$$\phi_e = \arctan\left(-S^{+}_{\mathrm{Imag,m}}/S^{+}_{\mathrm{Real,m}}\right). \tag{S23}$$

Supplementary Note IV : AC Bias Field Calibration, Target Signal Sensitivity Measurement, and Bias Field Polarization

The amplitude of the effective (measured) signal is proportional to the product of the target signal and AC bias field amplitudes, as described by Eq. (S14). Therefore, we carefully calibrate the bias field amplitude at each frequency to ensure that the sensitivity to the target signal of interest is accurately measured.

We first measure the reflection coefficient (S_{11}) of the RF coil and find it to be approximately flat across all frequencies of interest. Using a spectrum analyzer (Signal Hound USB-SA44B), we measure the output power of the RF amplifier and ensure consistent power delivery to the loop across all relevant frequencies and experimental conditions.

We calibrate the field amplitude by tuning this field's frequency to the NV resonant frequency $\omega_0 = \omega_{\text{-}1}$, driving NV Rabi oscillations (nutation), and measuring the Rabi frequency Ω_0. We then record the corresponding input power to the RF coil using the spectrum analyzer at the amplifier's output. Assuming equivalent S_{11} responses at both ω_0 and other values of ω_b, we determine the amplitude Ω_b at frequency ω_b to be equal to Ω_0 for equivalent input power. We investigate the validity of this assumption experimentally in Section V. For QFM-CASR sensitivity measurements, we calibrate the amplifier's power output (i.e., input to the RF coil) in order to keep a constant AC bias field amplitude across all measured frequencies. As the target RF signals used in this experiment are detuned from the AC bias field by only about 1 MHz, and are synthesized and delivered by the same AWG, amplifier and RF loop as the AC bias field, the above calibration procedure also ensures that the target signal amplitude is constant for a given input power to the RF coil across all relevant frequencies.

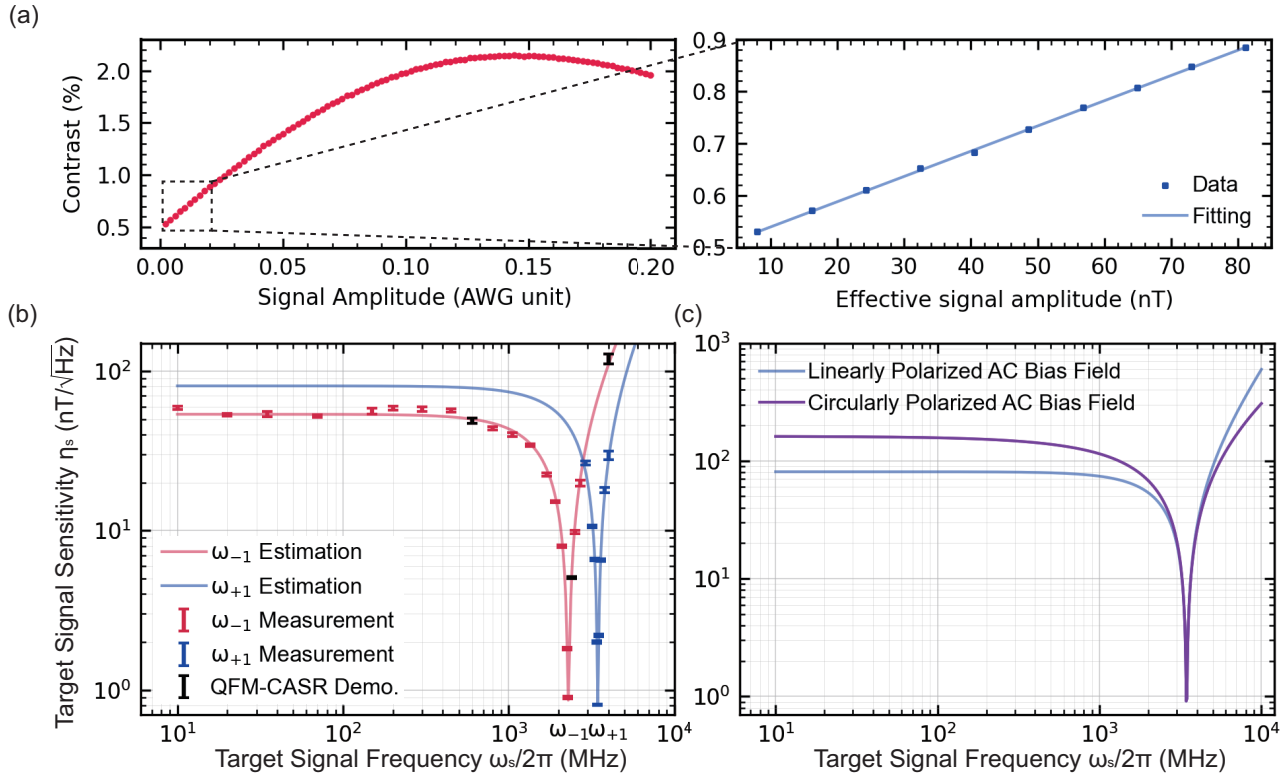


FIG. S2. (a) Demonstration of QFM-CASR sensitivity calibration measurement for a target signal at 2.4 GHz and an effective signal frequency ≈ 1 MHz. (b) Sensitivity assessment of QFM-CASR narrowband (AC) magnetometry, including measurement error bars, across a wide target signal frequency range of 10 MHz to 4 GHz. The data and estimations are the same as Fig. 2 in the main text. The error bars are derived from the standard deviation of 10 individual sensitivity measurements at each test frequency. (c) Comparison of the estimated sensitivity using a linearly polarized AC bias field (blue, same as the blue curve in (b)) and a circularly polarized AC bias field (purple), for the NV spin resonance frequency ω_{+1}. The use of a circularly polarized bias field provides a modest enhancement in sensitivity when $\omega_s > \omega_{+1}$.

We experimentally determine and theoretically estimate the QFM-CASR narrowband (AC) sensitivity using the methods described in sections IV C and II B of the main text, respectively. To illustrate the sensitivity calibration method, we present an example measurement for a target signal at 2.4 GHz, as shown in Fig. S2(a). After adjusting the effective signal to be in-phase with the XY8-6 sequence, i.e., $\phi_s - \phi_b = 0$, we determine the AC magnetometry curve for the effective signal (≈ 1 MHz) by fixing the signal phase ϕ_s, and the AC bias field phase ϕ_b and amplitude Ω_b, measuring the NV readout PL contrast from the XY8-6 sequence, and then repeating these measurements for iterated values of the AWG output amplitude A (effectively sweeping Ω_s) from zero to identify the first turning point, $A_{\pi/2}$, where the NV spin accumulates a $\pi/2$ dynamical phase. $A_{\pi/2} = 0.144$ AWG unit in this example. The AC magnetic field amplitude required to accumulate a $\pi/2$ phase is given by $B_{\pi/2} = \hbar\pi^2/(2g\mu_B N) = 0.58\,\mu$T. We obtain the calibration factor between the AWG amplitude and the signal amplitude, $B_{\pi/2}/A_{\pi/2} = 4.06\,\mu$T/AWG unit. We then perform a linear fit on the near-zero AWG output data (first 10 data points) of the AC magnetometry curve; and by applying the calibration factor, we determine the contrast slope $s = 4.86 \times 10^{-5}\,\text{nT}^{-1}$. Next, we run continuous QFM-CASR sensing for $t = 1$ s without the target signal to measure the contrast noise $\sigma = 4.57 \times 10^{-6}$; subsequently calculate the effective signal sensitivity $\eta_e = \sigma/s \cdot \sqrt{t} = 0.094\,\text{nT} \cdot \text{Hz}^{-1/2}$ and finally calculate the target signal sensitivity $\eta_s = 4.87\,\text{nT} \cdot \text{Hz}^{-1/2}$.

At each target signal frequency, we perform 10 sensitivity measurements and calculate the standard deviation, which determines the error bars shown in Fig. S2(b). For measurements at all target signal frequencies, we find an average percentage error $\overline{\sigma/\eta_s} \approx 2.7\,\%$. Given the careful calibration of the RF amplifier's output power, we attribute the small differences between the measured and estimated sensitivities to the frequency dependence of the RF coil, where the measured S_{11} response, while approximately flat from 10 MHz to 4 GHz, does exhibit variations $\sim 10\%$.

Fig. S2(c) compares the estimated QFM-CASR sensitivity of our experimental system with a linearly polarized AC bias field (as used in all measurements presented here) versus a circularly polarized AC bias field (not used experimentally in the present study). The sensitivity with linearly polarized AC bias and target signal fields is

computed from Eq. (S14), while the sensitivity with a circularly polarized AC bias field and a linearly polarized target signal field is calculated from:

$$\Omega_e = \frac{\Omega_b \Omega_s}{4}\left(\frac{1}{\omega_b - \omega_0} + \frac{1}{\omega_s - \omega_0}\right), \tag{S24}$$

where this expression is derived following a process similar to that of Sec. II and [1]. We note that a linearly polarized bias field achieves better sensitivity for target signals residing below the NV spin resonance ($\omega_s < \omega_0$), while a circularly polarized bias field is optimal for signals residing above the NV spin resonance ($\omega_s > \omega_0$). For NV spin resonance frequencies similar to those used in our experiment, i.e., for DC bias fields ~ 10 mT, a circularly polarized bias field is expected to provide about a factor-of-two enhancement in AC sensitivity over the linear case at 10 GHz target signal frequency.

Supplementary Note V: Effective Signal Validation with Rabi and DEER-Rabi

In the previous section, we assume that the amplitude of the applied AC bias field is constant and independent of frequency by ensuring that the output power of the RF amplifier is the same at all frequencies. Here, we verify this assumption in two regimes where we can measure the signal and bias fields directly without the use of QFM: near the lower NV spin resonance ($\omega_0 = \omega_{-1}$), we are able to directly measure the bias and signal field amplitudes via the induced NV Rabi nutation (oscillation) frequency; and near the ESR resonance (≈ 666 MHz) of paramagnetic nitrogen impurity (P1 centers) in the diamond, we can measure the bias and signal field amplitudes using a double electron-electron resonance (DEER) Rabi experiment [4, 5]. We also verify Eq. (S14) by comparing the effective signal field B_e measured by a QFM-XY8-6 AC magnetometry protocol with the effective signal field B'_e computed using Eq. (S14) and the bias and signal field amplitudes measured independently and without QFM using NV Rabi nutation.

We begin by performing QFM-XY8-6 AC magnetometry near 2.4 GHz, and also non-QFM measurements of the signal and AC bias field amplitudes via NV Rabi oscillation at the resonance frequency $\omega_{-1} \approx 2.29$ GHz. By applying a signal field at 2.4 GHz and a bias field at 2.399 GHz, a QFM-XY8-6 AC magnetometry curve for the effective field is recorded by sweeping the AWG output amplitude for the signal field while maintaining a constant bias field amplitude, as shown in Fig. S3(a). The AWG output amplitude corresponding to $\pi/2$ phase accumulation due to the effective field is identified by locating the maximum value of the magnetometry curve. This phase accumulation corresponds to a specific value of the effective field: $B_{\pi/2} = \hbar\pi^2/(2g\mu_B N) = 0.58(1)\,\mu$T, where $g \approx 2$ for NV, $N = 48$ is the number of π pulses in the XY8-6 sequence, and the uncertainty arises from sinusoidal fitting of the magnetometry curve. To calibrate the RF amplifier output power at the signal and bias field frequencies, we use the spectrum analyzer described in the previous section. The calibrated powers are then applied individually for the bias and signal fields at $\omega_{-1} \approx 2.29$ GHz, i.e., without QFM, to measure the NV Rabi oscillation frequencies generated by these fields. From these measurements, we determine $\Omega_b = (2\pi)4.310(6)$ MHz and $\Omega_s = (2\pi)0.841(2)$ MHz as shown in Fig. S3(b). Using these amplitudes in Eq.(S14), we find the computed effective field $B'_e \approx 0.57\,\mu$T. The observed $\sim 2\%$ discrepancy between the measured (B_e) and calculated (B'_e) effective field amplitudes is consistent with the uncertainty in identifying the AWG amplitude corresponding to $\pi/2$ phase accumulation in the QFM-XY8-6 AC magnetometry curve for the effective field (Fig. S3(a)). There is insignificant apparent contribution from any small differences in signal and bias field amplitudes at 2.29 GHz (where the NV Rabi oscillation measurements are performed) and near 2.4 GHz (where QFM-XY8-6 AC magnetometry is performed).

We perform a similar experiment using DEER Rabi magnetometry. As shown in Fig. S4(a), DEER consists of pulsed, near-resonant driving of the paramagnetic bath spins, which are primarily neutral substitutional ^{15}N (i.e., P1 centers, $S = 1/2$) for the diamond sample used in this work, while performing a simultaneous NV Hahn (i.e., spin) echo measurement. Recall that the π pulse in a Hahn echo sequence refocuses the spin magnetization of the NV ensemble under the assumption that the spin bath remains constant during the Hahn echo sequence, thereby extending the spin coherence lifetime of the NV ensemble from T_2^* (the dephasing time) to T_2 (the Hahn echo decoherence time). By applying a near-resonant RF pulse to the spin bath, centered in time around the Hahn echo pulse applied to the NVs, the spin bath magnetization is partially inverted simultaneously with the inversion of the NV magnetization. Thus, the dephasing effect due to the components of the spin bath inverted by the spin-bath RF pulse are not refocused during the NV Hahn echo, leading to a reduction of NV decoherence time T_2, which can be measured as a change in NV PL contrast.

The electron spin (ESR) transition frequencies for P1 centers in the diamond used in this experiment can be calculated from the ground-state Hamiltonian [4, 5]:

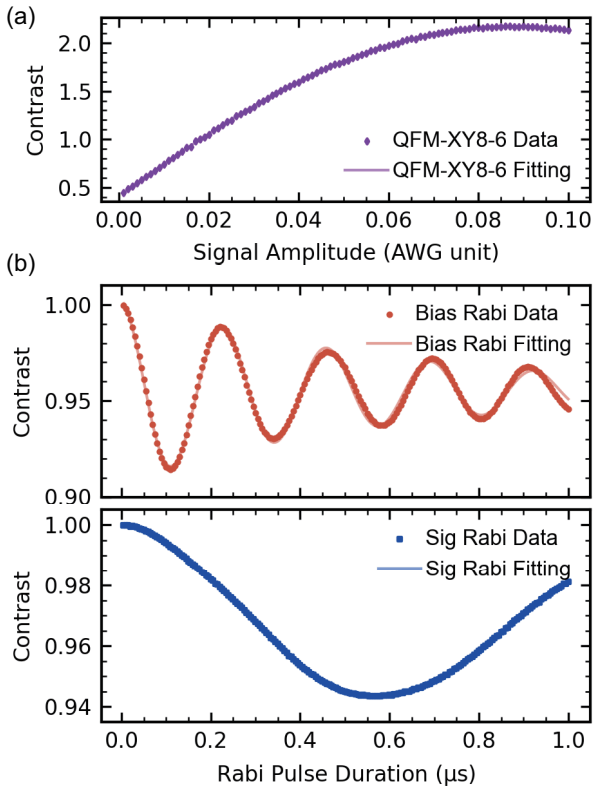


FIG. S3. (a) QFM-XY8-6 AC magnetometry curve for the effective field at 1 MHz, acquired by varying the target signal field amplitude while maintaining a constant AC bias field amplitude. Signal and bias are at 2.4 GHz and 2.399 GHz, respectively. The maximum value of the AC magnetometry curve corresponds to a $\pi/2$ NV phase accumulation due to the effective field, which is used to compute the effective field amplitude = 0.58(1) μT. (b) Fits to measurements of NV Rabi oscillation are used to determine the bias field amplitude $\Omega_b = (2\pi)4.310(6)$ MHz (upper plot) and the signal field amplitude $\Omega_b s = (2\pi)0.841(2)$ MHz (lower plot).

$$\frac{\hat{H}}{h} = \frac{\mu_B}{h}\vec{B}\cdot\overline{g}\cdot\vec{S} + \frac{\mu_N}{h}\vec{B}\cdot\vec{I} + \vec{S}\cdot\overline{A}\cdot\vec{I}, \tag{S25}$$

where μ_B is the Bohr magneton, h is the Planck's constant, $\vec{B} = (B_x, B_y, B_z)$ is the applied DC bias magnetic field vector, $\overline{g}$ is the electronic g-factor tensor, μ_N is the ^{15}N nuclear magneton, $\vec{\hat{S}} = (\hat{S}_x, \hat{S}_y, \hat{S}_z)$ is the dimensionless electronic spin vector, $\overline{A}$ is the hyperfine tensor, and $\vec{\hat{I}} = (\hat{I}_x, \hat{I}_y, \hat{I}_z)$ is the dimensionless nuclear spin vector. When the z-axis is chosen as one of the four NV crystal axis directions, tensors $\overline{g}$ and $\overline{A}$ are diagonal and defined by

$$\overline{g} = \begin{pmatrix} g_\perp & 0 & 0 \\ 0 & g_\perp & 0 \\ 0 & 0 & g_{||} \end{pmatrix}, \quad \overline{A} = \begin{pmatrix} A_\perp & 0 & 0 \\ 0 & A_\perp & 0 \\ 0 & 0 & A_{||} \end{pmatrix}, \tag{S26}$$

where $g_\perp$, $g_{||}$, $A_\perp$, and $A_{||}$ are the gyromagnetic and hyperfine on and off-axis components, respectively. ^{15}N has $S = 1/2$ and $I = 1/2$, leading to the four eigenstates $|m_S = \pm 1/2, m_I = \pm 1/2\rangle$. The two corresponding dipole-allowed transitions ($\Delta m_S = \pm 1$, $\Delta m_I = 0$, solid arrows), along with the two first-order forbidden transitions ($\Delta m_S = \pm 1$, $\Delta m_I = \pm 1$, dashed arrows) are shown in Fig. S4(a). Using $g_\perp = g_{||} = 2$, $A_\perp = -559.7$ MHz, $A_{||} = -113.83$ MHz [4], and $|\vec{B}| = 20.7$ mT aligned with one NV axis, we calculate the two allowed transition frequencies of the on-axis P1 centers as 665.5 MHz and 505.8 MHz. Fig. S4(b) shows a measured DEER spectrum of one of the allowed transitions. Fitting the DEER spectrum with a Lorentzian function, we acquire the P1 resonance frequency $f_{\mathrm{P1}} = 665.67(1)$ MHz, in good agreement with our calculation.

Sweeping the duration of the RF pulse at f_{P1} produces a Rabi nutation of the P1 centers, where the frequency of this Rabi oscillation yields the RF pulse amplitude. We use this approach to directly measure the amplitudes of the

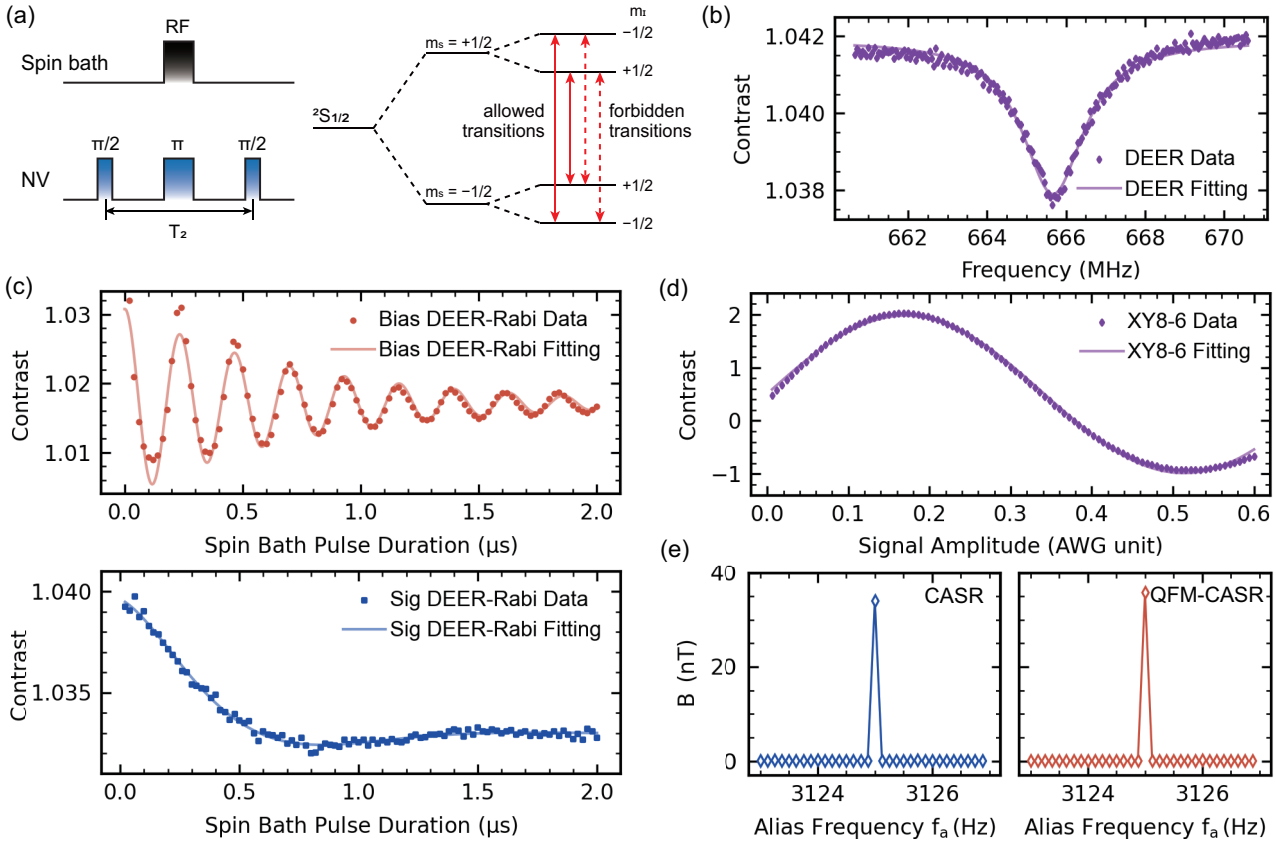


FIG. S4. (a) Schematic of the DEER pulse sequence. A near-resonant RF pulse (black) is applied to the paramagnetic bath spins in the diamond sample (primarily substitutional ^{15}N atoms, i.e., P1 centers) simultaneously with an NV Hahn echo measurement (blue), causing a reduction in the NV decoherence time T_2. The energy diagram of allowed (solid line) and forbidden (dotted line) ^{15}N spin transitions is shown to the right. (b) DEER spectrum is measured by sweeping the frequency of a weak RF pulse around the 666 MHz on-axis ^{15}N transition. The P1 resonance frequency $f_{\mathrm{P1}} = 665.67$ MHz is determined from a Lorentzian fit to the DEER data. (c) DEER-Rabi performed using either the AC bias field to provide the DEER RF pulse at f_{P1} (red) or the signal field (blue). In each case, data is acquired by sweeping the duration of the spin-bath RF pulse. Data is fit to an exponentially-damped sinusoid with a contrast offset. (d) Example XY8-6 AC magnetometry curve (non-QFM) from measurements of a 1 MHz test signal and a fit to a sinusoid with offsets, used to calibrate the ratio of applied RF signal amplitude and AWG output amplitude. (e) (left) CASR (non-QFM) spectrum of a 1 MHz+3.125 kHz signal with 0.1 AWG output amplitude, corresponding to a 34.1(1) nT RF signal amplitude based on the calibration performed in (d). (right) QFM-CASR spectrum of the effective signal resulting from applying signal and bias fields at 666 MHz+3.125 kHz and 665 MHz with the amplitudes shown in (c). The effective signal amplitude is determined to be 37.4(1) nT based on the CASR calibration.

target signal and AC bias fields, with each field applied alone and serving as the spin-bath RF pulse in the DEER-Rabi measurement, using the same amplifier output powers for these fields as in the previous NV Rabi measurements (Fig. S3(b)). As shown in Fig. S4(c), the DEER-Rabi frequency for the AC bias field is determined to be 4.30(1) MHz, indicating that the AC bias field amplitude at 665.67 MHz is in good agreement with the value obtained using NV Rabi at 2.29 GHz. The DEER-Rabi frequency for the target signal field is determined to be 0.56(3) MHz, indicating $\sim$ 30% systematic discrepancy between the two caibration techniques (NV Rabi at 2.29 GHz and DEER-Rabi at 666 MHz) at the order-of-magnitude lower RF amplitude used for target signal fields, compared to AC bias fields. Note that experiments to calibrate QFM-CASR sensitivity assume constant AC bias field amplitude as a function of frequency; but do not do not require maintaining a constant target signal amplitude across all frequencies.

We also perform QFM-CASR measurements of the effective signal field B_e near 666 MHz. The target signal field is at 666 MHz + 3.125 kHz with amplitude of 0.56(3) MHz determined from a DEER-Rabi measurement; and the AC bias field is at 665 MHz, with amplitude of 4.30(1) MHz also measured using DEER-Rabi. We acquire QFM-CASR time-domain data for the effective signal and determine the QFM-CASR spectrum (see Fig. S4(e)). To calibrate the QFM-CASR spectrum, we perform a standard XY8-6 AC magnetometry measurement (no QFM or CASR) by applying a 1 MHz test signal delivered to the NV ensemble with the same RF coil used for all other measurements,

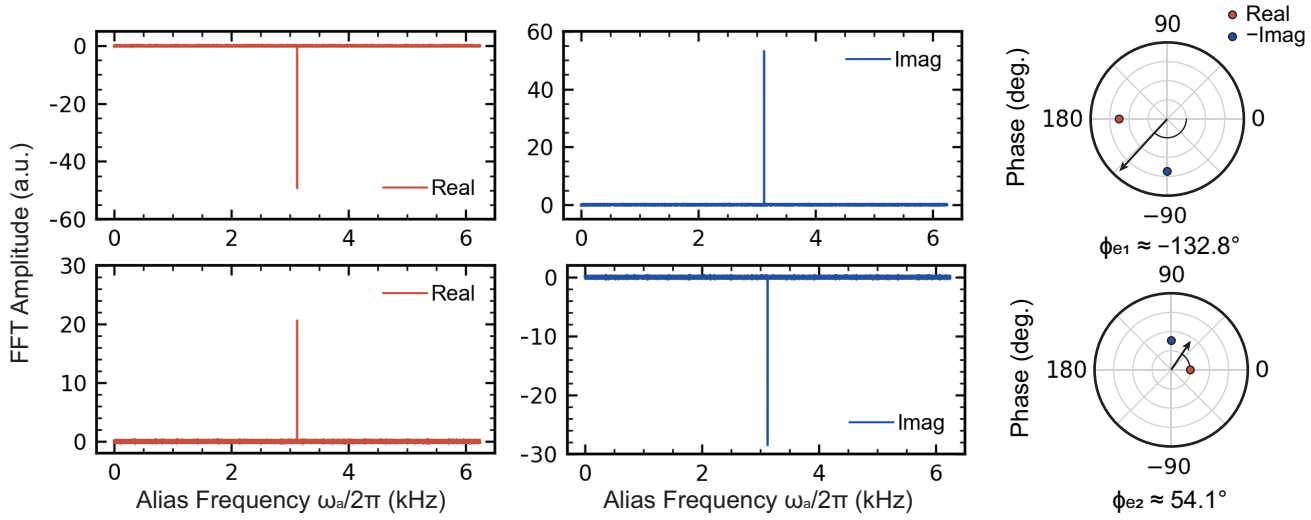


FIG. S5. Precise QFM-CASR phase measurements of target signals near 666 MHz (top) and 4 GHz (bottom). For the experiment near 666 MHz, the same data set is used as in producing the QFM-CASR spectrum shown in Fig. S4(e). For the experiment near 4 GHz, the same $\Omega_{b,s}$ is applied as for the 666 MHz experiment, with $\omega_s = (2\pi)(4\,\text{GHz} + 3.125\,\text{kHz})$ and $\omega_b = (2\pi)3.999\,\text{GHz}$. Real (red) and imaginary (blue) components of the QFM-CASR spectra are displayed, as generated from FFT of time-domain QFM-CASR data (NV PL measurements). Polar plots illustrate the phases of each effective signal, as derived from QFM-CASR measurements. Red and blue dots represent the real and imaginary amplitudes of the associated QFM-CASR spectra, respectively, while black arrows indicate the absolute value of the amplitude. Grids are shown as circles with a radial step size equivalent to 20 arbitrary units of FFT amplitude.

as shown in Fig. S4(d), and obtain a calibration factor of $B/A = 341(1)\,\text{nT}$, where B is the amplitude of the 1 MHz test signal determined from the XY8-6 AC magnetometry measurements and A is the AWG output amplitude. Following this calibration, we measure the CASR (non-QFM) spectrum using a $1\,\text{MHz} + 3.125\,\text{kHz}$ test signal at 0.1 AWG output amplitude, as shown in Fig. S4(e). Using the B/A calibration factor, the CASR signal amplitude is determined to be $34.1(1)\,\text{nT}$. Comparing the experimentally-determined QFM-CASR and CASR amplitudes, we obtain $B_e = 37.4(1)\,\text{nT}$. Using Eq. (S14) and the signal and bias amplitudes near 666 MHz, measured via DEER-Rabi, we calculate $B'_e \approx 40\,\text{nT}$. The discrepancy $\sim 8\%$ between B_e and B'_e is attributed to DEER-Rabi measurement error for the weak signal field. Note also that B_e is two orders of magnitude smaller than the value determined above when the signal and bias fields are near 2.4 GHz ($B_e \approx 0.58\,\mu\text{T}$), consistent with expected QFM behavior far from the NV resonances.

Supplementary Note VI: Phase Measurements of Arbitrary Frequency Signals

In Sec. II D of the main text, we claim that precise phase measurement can be implemented with QFM-CASR by applying an AC bias field of known phase close to the target RF signal frequency; and we then demonstrate such phase measurement for a signal near 2.4 GHz. Here, we demonstrate precise QFM-CASR phase measurement near two additional frequencies, 666 MHz and 4 GHz. We use AC bias phases $\phi_{b1} = \phi_{b2} = 0$ at both frequencies; and applied target signal phases $\phi_{s1} = -133°$ at 666 MHz and $\phi_{s2} = 54°$ at 4 GHz.

The phase of the effective signal ϕ_e is determined from the ratio of the real and imaginary components of the QFM-CASR spectrum (see Fig. S5). The experimental target signal phase ϕ'_s is then extracted via the relationship $\phi'_s = \phi_e + \phi_b$. From our measurements, we determine $\phi'_{s1} \approx -132.8°$ and $\phi'_{s2} \approx 54.1°$, in good agreement with the applied target signal phases.

Supplementary Note VII: Comparison of NV-Diamond AC Sensing Techniques

In Sec. III of the main text, we compare the sensitivity and signal frequency range of the QFM-CASR magnetic spectroscopy protocol with state-of-the-art AC magnetometry experiments and techniques using NV ensembles in diamond. In Fig. S6, we provide a graphical comparison of sensitivity vs. target signal frequency for QFM-CASR and the NV-diamond AC sensing experiments reported in [7–12], including both NV ensemble and single NV results.

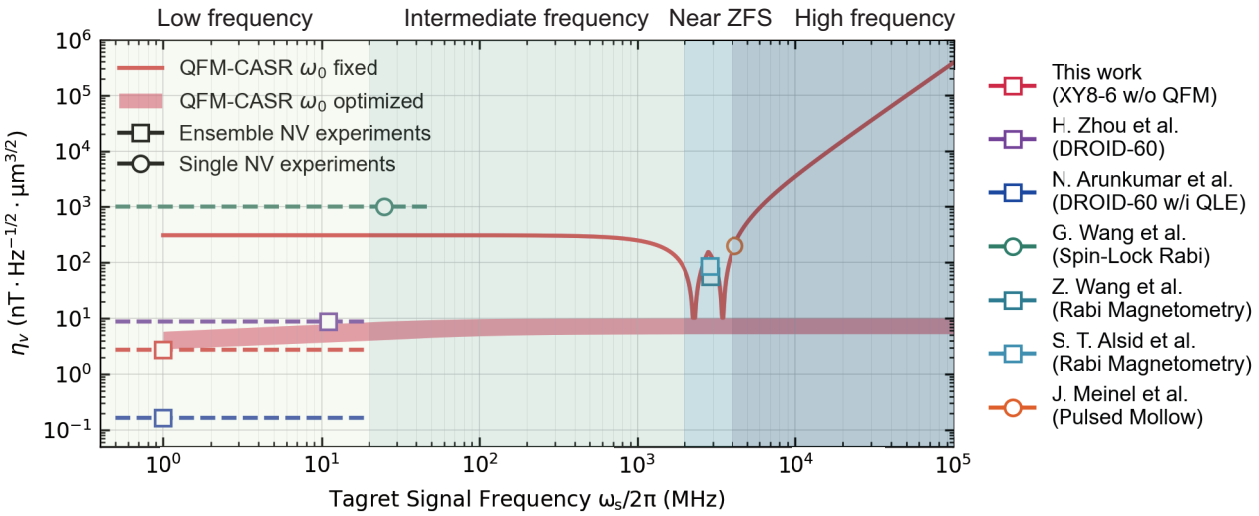


FIG. S6. Comparison of narrowband (AC) volume-normalized sensitivity and applicable signal frequency range for state-of-the-art NV-diamond experiments, including the present QFM-CASR results (ω_0 fixed, solid red line) and optimized QFM-CASR (red band). For non-QFM results at lower signal frequencies, the square or circular symbol indicates the reported sensitivity and detected signal frequency, and the flat dashed line indicates the signal frequency range of the technique. All these non-QFM techniques have AC sensitivity that varies with signal frequency, typically degrading at frequencies higher or lower than the values indicated by the symbols [6].

For ensemble NV experiments, the sensing volume V and diamond properties vary significantly. To facilitate comparison, we normalize their sensitivities by the sensing volume, defining $\eta_v = \eta \cdot \sqrt{V}$ (the "volume-normalized sensitivity"). For single NV experiments, we assume a sensing volume of $V = 1\,\mu\text{m}^3$ to allow a consistent comparison. The sensitivity of the QFM-CASR protocol depends on both the NV resonant frequency and the AC bias field amplitude, as described in Eq. (S14). For this analysis, we estimate the optimized QFM-CASR sensitivity (as shown by the red band in Fig. S6) by assuming (i) an adjustable DC bias magnetic field is applied to Zeeman shift the NV spin resonance ω_0 to be near the signal frequency while maintaining the far-detuning assumption of the QFM effect, i.e., $|\omega_0 - \omega_b| > \Omega_{b,\text{max}}$; and (ii) a large AC bias field is applied for all frequencies, with $\Omega_{b,\text{max}} = (2\pi)20\,\text{MHz}$.

In the low-frequency regime ($< 20\,\text{MHz}$), the QFM-CASR AC sensitivity realized in the present study, with DC bias field and ω_0 fixed (red line in Fig. S6), is more than two orders of magnitude worse than that of dynamical decoupling sequences such as XY8 and DROID-60 [7, 8]. While the use of a large DC bias magnetic field ($\sim$95 mT) can improve the QFM-CASR sensitivity to within an order of magnitude of that of XY8 by tuning the NV resonances within $\sim 20\,\text{MHz}$ of the target signal frequency, implementing such large magnetic fields is technically challenging and adds significant experimental complexity. As a result, dynamical decoupling sequences remain the preferred choice for low-frequency signals.

Near the NV zero-field splitting (ZFS, 2.87 GHz), Rabi magnetometry [10, 11] has similar sensitivity to QFM-CASR. However, Rabi magnetometry is limited to spectral resolution in the kHz range, which cannot match the sub-Hz resolution of QFM-CASR. Techniques such as heterodyne detection spectroscopy based on the Mollow triplet [12] offer sub-Hz resolution but still require the signal frequency to be within a few MHz from the NV spin resonance, limiting the signal frequency range to approximately 100 MHz without changes to the DC bias field. By contrast, the QFM-CASR protocol achieves comparable sensitivities while providing a significantly extended signal frequency range.

In the intermediate frequency regime (20 MHz to 2 GHz) and at higher frequencies ($> 4\,\text{GHz}$), QFM-CASR is the only currently viable technique for sensitive, high-spectral-resolution NV measurements of narrowband signals. Although Rabi magnetometry could theoretically address these frequencies under extreme conditions, e.g., with DC bias fields $> 100\,\text{mT}$, QFM-CASR achieves comparable sensitivity while offering a broader signal frequency range and reduced experimental complexity.

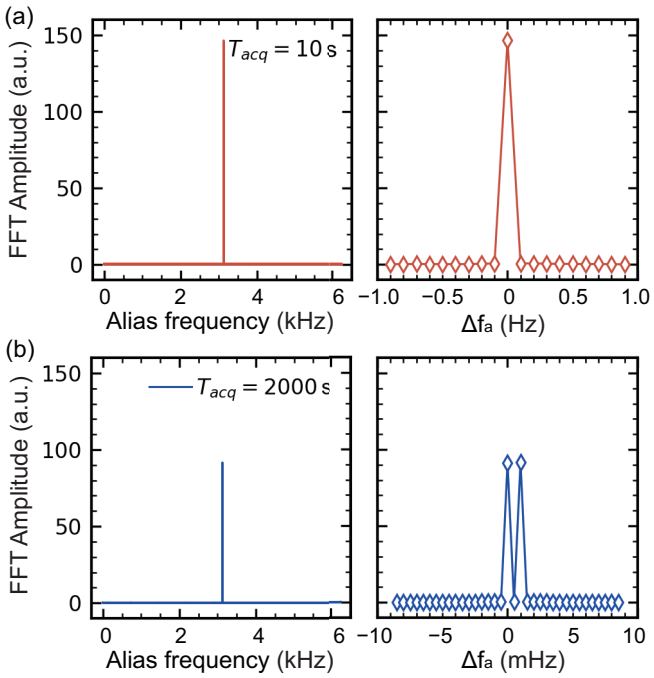


FIG. S7. Demonstration of sub-Hz QFM-CASR spectral resolution with two test signals near 2.4 GHz + 3.125 kHz having a frequency difference of 1 mHz. (a) For $T_{\rm acq} = 10$ s, $\delta f \approx 100$ mHz, and the contributions of the two signals merge into a single peak in an FFT of QFM-CASR time-domain data. (b) For $T_{\rm acq} = 2000$ s, $\delta f \approx 0.5$ mHz, and the two signal frequencies are resolved, showing a 1 mHz difference.

Supplementary Note VIII: Demonstration of Sub-Hz QFM-CASR Spectral Resolution

In spectroscopy, the frequency resolution $\delta f \approx 1/t_{\rm acq}$, where $t_{\rm acq}$ is the total acquisition time of the time-domain data, i.e., NV photoluminescence (PL) in this work. In Sec. II C of the main text, we demonstrate 8 s measurement time-domain QFM-CASR data (Fig. 3(b)), which is sufficiently long (> 2 s) to achieve sub-Hz spectral resolution. Here, we provide additional data to support this capability.

In principle, the spectral resolution of the QFM-CASR protocol can be arbitrarily high, as $t_{\rm acq}$ is not limited by the NV spin lifetime [2]. Here, we perform experiments to distinguish two target signals with a frequency difference of 1 mHz, with results shown in Fig. S7. We apply two signals at frequencies $f_{s1} = 2.4\,{\rm GHz} + 3.125\,{\rm kHz}$ and $f_{s2} = f_{s1} + 1\,{\rm mHz}$, with the AC bias field at $f_b = 2.399\,{\rm GHz}$. We first employ an acquisition time $t_{\rm acq} = 10\,{\rm s}$, such that $\delta f \approx 100\,{\rm mHz}$. The resulting FFT of the QFM-CASR time-domain data shows a single peak contributed by both signals: i.e., the two signals are not resolved, as expected. We next perform a QFM-CASR experiment with $t_{\rm acq} = 2000\,{\rm s}$, the two signals with a 1 mHz frequency difference are resolved, demonstrating a spectral resolution $\approx 0.5\,{\rm mHz}$.

The acquisition time $t_{\rm acq}$ is ultimately limited by systematic drift of the experimental setup (on the timescale of tens of hours). Thus, the spectral resolution of the QFM-CASR protocol is sufficiently high for most potential applications.

Supplementary Note IX: Demonstration of QFM-CASR at 2.5 MHz AC Bias Field Detuning

In the experiments reported elsewhere in this manuscript , we set the AC bias field detuning from the target signal to 1 MHz because this detuning optimizes sensitivity of the XY8-6 measurement sequence for our NV-diamond sample. However, the QFM-CASR technique is not limited to 1 MHz detuning, which determines the frequency of the effective signal; rather it is constrained by the sensing frequency range of dynamical decoupling sequences (typically $\lesssim 20\,{\rm MHz}$).

To demonstrate the versatility of the QFM-CASR protocol in detecting target RF signals with different effective signal frequencies, we perform an experiment with an AC bias field detuning (i.e., effective signal frequency) of 2.5 MHz, as shown in Fig. S8. In this experiment, we apply a target signal similar to Sig1 in Fig. 3 of the main text: $\omega_s = (2\pi)2.4005\,{\rm GHz}$, $\Omega_s = (2\pi)0.21\,{\rm MHz}$ ($B_s = 7.5\,\mu{\rm T}$). We apply an AC bias field with a detuning of 2.5 MHz

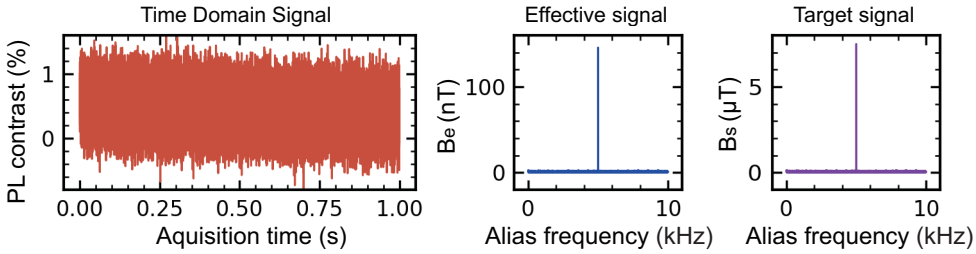


FIG. S8. Demonstration of QFM-CASR with AC bias field detuned by 2.5 MHz from target signal field. Experimental parameters are: $\omega_s = (2\pi)(2.4005\,\text{GHz})$, $\Omega_s = (2\pi)0.21\,\text{MHz}$ ($B_s = 7.5\,\mu\text{T}$); $\omega_b = (2\pi)2.3975\,\text{GHz}$, $\Omega_b = (2\pi)4.3\,\text{MHz}$ ($B_b = 153.4\,\mu\text{T}$). Left to right: 1-second measurement of QFM-CASR time-domain data (red), Fourier spectrum of effective signal (blue), and spectrum of target signal (purple).

but the same amplitude as in Fig. 3 of the main text: $\omega_b = (2\pi)2.3975\,\text{GHz}$, $\Omega_b = (2\pi)4.3\,\text{MHz}$ ($B_b = 153.4\,\mu\text{T}$). To maintain resonance with the XY8-6 sequence, we adjust the π pulse spacing to $\tau = 0.2\,\mu\text{s}$, enabling a shorter measurement sequence length of $T_{seq} = 50\,\mu\text{s}$, which results in a broader CASR bandwidth of 10 kHz and a CASR alias frequency ≈ 5 kHz for the 2.5 MHz effective signal frequency. Based on Eq. (S14), modifying the AC bias field frequency detuning on the scale of MHz does not significantly change the ratio between the effective signal and the target signal ($\approx 0.7\%$ change in this ratio). The measured time-domain QFM-CASR signal and the resulting QFM-CASR Fourier spectra of both the effective and target signals are shown in Fig. S8.

Supplementary Note X: QFM-CASR Performance Limitations, Trade-Offs, and Optimization

The performance of the QFM-CASR spectroscopy technique is characterized by signal frequency range, sensitivity, detection bandwidth, and spectral resolution.

In this work, we experimentally demonstrate QFM-CASR measurements across a signal frequency range of about 4 GHz, more than an order of magnitude greater than other NV AC sensing techniques. However, there is no fundamental limitation preventing further extension of this range. The primary technical constraint arises from the bandwidth of our current amplifier (see details in Sec. I), which could be overcome by employing a higher-frequency amplifier. Another challenge stems from the weak effective signal when the target frequency is significantly different from the NV resonant frequency, leading to rapid sensitivity degradation at higher frequencies (see Fig. 2 of the main text and Fig. S6). This issue can be mitigated by increasing the bias magnetic field to increase the NV ω resonant frequency and compensate for the frequency difference.

The sensitivity of the QFM-CASR technique is determined by both the (conventional) AC sensitivity of the dynamical decoupling sequence, as well as the quantum frequency mixing factor (Eq. S14). For the NV-diamond sample used in this work, the XY8-6 dynamical decoupling sequence achieves optimal sensitivity when the effective signal frequency is approximately 1 MHz [13]. As with all NV dynamical decoupling protocols, this sensitivity varies significantly across its detection frequency range $\lesssim 20$ MHz [6]. The quantum frequency mixing effect greatly increases the signal frequency range (as discussed above) while providing sub-Hz spectral resolution; but reduces effective signal sensitivity by an order of magnitude or more (as shown in Fig. S6). To optimize detectability of the effective signal with QFM-CASR, a strong AC bias field can be applied, with the NV resonant frequency tuned close to the target signal frequency.

The QFM-CASR detection bandwidth is approximately $1/(2T_{seq})$, where T_{seq} is the measurement sequence length (see Fig. 3(a) of the main text). There is an inherent trade-off between QFM-CASR sensitivity and detection bandwidth. To optimize sensitivity, we employ a many-pulse dynamical decoupling sequence (XY8-6) with an AC bias field detuned from the target signal field by ≈ 1 MHz, rather than a simpler sequence such as Hahn spin echo with a larger detuning and hence higher effective signal frequency. While this choice improves sensitivity, it increases the sequence length (T_{seq}) and thereby narrows the detection bandwidth. Under fixed laser power, reducing the NV spin initialization time could reduce T_{seq} and broaden the detection bandwidth, but this would also reduce readout contrast and sensitivity.

The spectral resolution of the QFM-CASR protocol is set by the inverse of the overall measurement time [2]; it is not limited by the NV spin state lifetime, as reinitialization typically becomes significant in each readout cycle. In our experiment, we demonstrate spectroscopy of a test signal generated by an AWG with constant amplitude and

frequency-stabilized by the AWG's crystal oscillator. QFM-CASR spectral resolution is ultimately constrained by systematic drift in instrumentation (such as the AWG crystal oscillator), which occur on a timescale of tens of hours. As demonstrated in Sec. VIII, achieving sub-Hz or even mHz spectral resolution is straightforward with QFM-CASR. However, for applications such as NV-NMR spectroscopy of small samples, the useful QFM-CASR spectral resolution will ultimately depend on the sample's NMR linewidth [2, 14, 15].

Supplementary Note XI: Assessment of QFM-CASR Applied to Tesla-Scale NMR of Micron-Scale Samples

We recapitulate the analysis and results from our previous work on micron-scale NV-NMR [2, 14, 15], now assuming a bias magnetic field of 1 T and NV-NMR signals detected using QFM-CASR. We estimate the NMR magnetic signal amplitude generated by Larmor-precessing protons in the sample, and measured at a test point in the NV ensemble sensor, by integrating over the average proton magnetic dipole moment for each point in the sample volume. Projecting the magnetic field from each sample dipole element onto the NV axis, we obtain

$$\mathbf{B}\cdot\hat{n}_{NV} = \frac{\mu_0\rho_{\rm th}}{4\pi}\int \frac{1}{r^3}\left[3(\hat{r}\cdot\mathbf{m}(t))(\hat{r}\cdot\hat{n}_{NV}) - (\mathbf{m}(t)\cdot\hat{n}_{NV})\right]dV, \tag{S27}$$

where $\rho_{\rm th}$ is the equilibrium number density of thermally-polarized protons in the sample, $\hat{r}$ is a unit vector along the direction connecting the test point and the infinitesimal sample volume, $\hat{n}_{NV}$ is a unit vector parallel to the NV axis, and $\mathbf{m}(t)$ is the time-varying dipole magnetic moment vector of the precessing proton spins.

We divide the proton magnetic moment into a direction $\hat{m}$ and magnitude γ_p, and pull the latter out of the integral such that all dimensions are collected in a prefactor:

$$\mathbf{B}\cdot\hat{n}_{NV} = C\int \frac{1}{r^3}\left[3(\hat{r}\cdot\hat{m}(t))(\hat{r}\cdot\hat{n}_{NV}) - (\hat{m}(t)\cdot\hat{n}_{NV})\right]dV. \tag{S28}$$

The prefactor that determines the approximate scale of the NMR magnetic field produced by the sample is

$$C = \frac{\mu_0\gamma_p}{4\pi}\rho_{\rm Tot}\left[1-\exp\left(-\frac{2\gamma_p B_0}{k_B T}\right)\right] \approx \frac{\mu_0\gamma_p}{4\pi}\rho_{\rm Tot}\frac{2\gamma_p B_0}{k_B T}, \tag{S29}$$

where $\rho_{\rm Tot}$ is the full number density of protons in the sample (taken here to be pure water), k_B is the Boltzmann constant, T is temperature, and the bias magnetic field $B_0 = 1\,\mathrm{T}$. Numerically, we obtain

$$C = \frac{\mu_0\gamma_p 2\rho_{\rm Tot}B_0}{2\pi k_B T} \tag{S30}$$

$$= \frac{(4\pi\times10^{-7}\,\mathrm{T\cdot m/A})(1.41\times10^{-26}\mathrm{A\cdot m^2})^2(6.6\times10^{28}\mathrm{m^{-3}})(1\,\mathrm{T})}{2\pi(1.38\times10^{-23}\mathrm{T\cdot A\cdot m^2/K})(300\mathrm{K})} \approx 640\ \mathrm{pT}. \tag{S31}$$

Next, we evaluated the dimensionless integral in Eq. (S28). The z-axis is taken to be perpendicular to the diamond surface. We define

$$\hat{\mu}_{NV} = \left(\frac{\sqrt{2}}{3}, 0, \frac{1}{\sqrt{3}}\right), \tag{S32}$$

as well as two perpendicular unit vectors,

$$\hat{q}_1 = \left(\frac{1}{\sqrt{3}}, 0, -\frac{\sqrt{2}}{3}\right), \quad \hat{q}_2 = (0,1,0), \tag{S33}$$

that describe the plane in which the nuclear spins precess when the bias field $\mathbf{B}_0$ is aligned parallel to the NV axis. Thus, the proton magnetization vector is

$$\hat{m}(t) = \hat{q}_1 \cos(\omega t) + \hat{q}_2 \sin(\omega t). \tag{S34}$$

The volume integral

$$G = \int \frac{dV}{r^3}[3(\hat{r}\cdot\hat{m}(t))(\hat{r}\cdot\hat{n}_{NV}) - (\hat{m}(t)\cdot\hat{n}_{NV})]. \tag{S35}$$

.

For a hemispherical sample volume on the diamond surface, the asymptotic value of G is ~ 1.4, giving a predicted NMR signal amplitude $\approx 1\,\mathrm{nT}$.

With $B_0 = 1\,\mathrm{T}$, the NV resonant frequency between the $|0\rangle$ and $|-1\rangle$ states is given by $\omega_0 = \gamma_e B_0 - D \approx (2\pi)25.2\,\mathrm{GHz}$, where $D = (2\pi)2.87\,\mathrm{GHz}$ is the zero-field splitting of the NV^- ground state, and $\gamma_e = (2\pi)28.024\,\mathrm{GHz/T}$ is the electron gyromagnetic ratio. The proton spin Larmor precession frequency is $\omega_s = \gamma_p B_0 \approx (2\pi)42.6\,\mathrm{MHz}$, where $\gamma_p = 42.577\,\mathrm{MHz/T}$ is the proton gyromagnetic ratio.

Based on the experimental demonstration in this paper, we can perform QFM-CASR detection of this NMR signal by applying an AC bias field with $\omega_b = (2\pi)41.6\,\mathrm{MHz}$ and $\Omega_b = (2\pi)4.3\,\mathrm{MHz}$. According to Eq. (S14), the estimated QFM-CASR sensitivity for the NMR signal is $\eta_{est} \approx 500\,\mathrm{nT}\cdot\mathrm{Hz}^{-1/2}$. To detect a 1 nT NMR signal with SNR = 1, an averaging time about 70 hours is thus required — nearly three days.

However, technical advances can significantly reduce this required signal averaging time. For example, it is feasible to increase the NV sensing volume by a factor of 10 (e.g., from the 1.7 μm layer in the current experiment to a 20 μm layer) and also increase the AC bias field amplitude by a factor of 3 (to $\Omega_b \approx (2\pi)13\,\mathrm{MHz}$), which would result in an order-of-magnitude improvement in sensitivity to $\sim 50\,\mathrm{nT}\cdot\mathrm{Hz}^{-1/2}$, reducing the averaging time for QFM-CASR detection of a micron-scale, thermally-polarized water NMR signal (SNR = 1) to < 1 hour. In addition, implementing quantum logic enhanced sensing (i.e., repetitive readout) [8] could provide another order-of-magnitude enhancement in sensitivity to $\sim 5\,\mathrm{nT}\cdot\mathrm{Hz}^{-1/2}$ at $B_0 = 1\,\mathrm{T}$, further reducing the averaging time to ~ 25 sec. It should also be straightforward to implement hyperpolarization techniques such as Overhauser DNP [15] to increase the NMR signal amplitude by more than two orders of magnitude. All together, these enhancements project to high-resolution QFM-CASR detection of a hyperpolarized proton NMR signal (SNR = 1) at $B_0 = 1\,\mathrm{T}$ from dilute molecules in solution at a concentration $\sim 20\,\mathrm{mM}$ in ~ 1 hour of signal averaging time. We plan to pursue such advancements in future work.

[1] G. Wang, Y. X. Liu, J. M. Schloss, S. T. Alsid, D. A. Braje, and P. Cappellaro, Sensing of arbitrary-frequency fields using a quantum mixer, Physical Review X **12**, 021061 (2022).

[2] D. R. Glenn, D. B. Bucher, J. Lee, M. D. Lukin, H. Park, and R. L. Walsworth, High-resolution magnetic resonance spectroscopy using a solid-state spin sensor, Nature **555**, 351 (2018).

[3] Z. Yin, J. Tang, C. A. Hart, J. W. Blanchard, X. Xiang, S. Satyajit, S. Bhalerao, T. Tao, S. J. DeVience, and R. L. Walsworth, Quantum diamond microscope for narrowband magnetic imaging with high spatial and spectral resolution, Phys. Rev. Appl. **22**, 054050 (2024).

[4] E. Bauch, C. A. Hart, J. M. Schloss, M. J. Turner, J. F. Barry, P. Kehayias, S. Singh, and R. L. Walsworth, Ultralong dephasing times in solid-state spin ensembles via quantum control, Phys. Rev. X **8**, 031025 (2018).

[5] J. Tang, Z. Yin, C. A. Hart, J. W. Blanchard, J. T. Oon, S. Bhalerao, J. M. Schloss, M. J. Turner, and R. L. Walsworth, Quantum diamond microscope for dynamic imaging of magnetic fields, AVS Quantum Science **5**, 044403 (2023).

[6] J. F. Barry, J. M. Schloss, E. Bauch, M. J. Turner, C. A. Hart, L. M. Pham, and R. L. Walsworth, Sensitivity optimization for nv-diamond magnetometry, Rev. Mod. Phys. **92**, 015004 (2020).

[7] H. Zhou, J. Choi, S. Choi, R. Landig, A. M. Douglas, J. Isoya, F. Jelezko, S. Onoda, H. Sumiya, P. Cappellaro, H. S. Knowles, H. Park, and M. D. Lukin, Quantum metrology with strongly interacting spin systems, Physical Review X **10**, 031003 (2020).

[8] N. Arunkumar, K. S. Olsson, J. T. Oon, C. A. Hart, D. B. Bucher, D. R. Glenn, M. D. Lukin, H. Park, D. Ham, and R. L. Walsworth, Quantum logic enhanced sensing in solid-state spin ensembles, Physical Review Letters **131**, 100801 (2023).

[9] G. Wang, Y.-X. Liu, Y. Zhu, and P. Cappellaro, Nanoscale vector ac magnetometry with a single nitrogen-vacancy center in diamond, Nano Letters **21**, 5143 (2021), pMID: 34086471.

[10] Z. Wang, F. Kong, P. Zhao, Z. Huang, P. Yu, Y. Wang, F. Shi, and J. Du, Picotesla magnetometry of microwave fields with diamond sensors, Sci. Adv **8**, 8158 (2022).

[11] S. T. Alsid, J. M. Schloss, M. H. Steinecker, J. F. Barry, A. C. Maccabe, G. Wang, P. Cappellaro, and D. A. Braje, Solid-state microwave magnetometer with picotesla-level sensitivity, Phys. Rev. Appl. **19**, 054095 (2023).

[12] J. Meinel, V. Vorobyov, B. Yavkin, D. Dasari, H. Sumiya, S. Onoda, J. Isoya, and J. Wrachtrup, Heterodyne sensing of microwaves with a quantum sensor, Nature Communications **12**, 2737 (2021).
[13] E. V. Levine, M. J. Turner, P. Kehayias, C. A. Hart, N. Langellier, R. Trubko, D. R. Glenn, R. R. Fu, and R. L. Walsworth, Principles and techniques of the quantum diamond microscope, Nanophotonics **8**, 1945 (2019).
[14] N. Arunkumar, D. B. Bucher, M. J. Turner, P. Tomhon, D. Glenn, S. Lehmkuhl, M. D. Lukin, H. Park, M. S. Rosen, T. Theis, and R. L. Walsworth, Micron-scale nv-nmr spectroscopy with signal amplification by reversible exchange, PRX Quantum **2**, 010305 (2021).
[15] D. B. Bucher, D. R. Glenn, H. Park, M. D. Lukin, and R. L. Walsworth, Hyperpolarization-enhanced nmr spectroscopy with femtomole sensitivity using quantum defects in diamond, Physical Review X **10**, 021053 (2020).